Analysis of the plasma discharge in a radio-frequency ion thruster chamber

IEPC-2024-329

Presented at the 38th International Electric Propulsion Conference, Toulouse, France
June 23-28, 2024

Simone Dalle Fabbriche* , Jiewei Zhou† , Jesús Perales-Díaz‡ , Eduardo Ahedo§
Department of Aerospace Engineering, Universidad Carlos III de Madrid, Leganes, Spain
Kristof Holste¶
Justus Liebig University Giessen

A 2D axisymmetric hybrid code has been used to study the discharge chamber in a radio-frequency ion thruster (RIT). This approach facilitates extensive parametric studies to determine optimal design parameters. Analyzing this region is crucial, as it is responsible for ionization and wall losses. To simulate the ion extraction system, a semi-transparent surface has been implemented. This study aims to present new RIT simulations and provide an overview of the plasma discharge inside the chamber, with a parenthesis on the effects of different grid transparencies on thruster performance. 2D maps of main plasma magnitudes are presented for different values of input power and injected mass flow rate. Additionally, current and energy flux to the walls have been analyzed and discussed. A preliminary analysis of the influence of transparency on efficiencies reveals a significant impact of this parameter. Finally, the results are compared against the global model developed at Giessen University, showing a very good agreement.

Nomenclature

h_x = weight for spatial distribution along x-th direction
I = current
j_k = current density of the k-th species
$\dot{m}$ = mass flow rate
n_k = density of the k-th species
P = power
T_e = electron temperature
α_w = wall accomodation factor
η = efficiency
ϕ = electric potential
P_k'' = energy flux to the walls of the k-th species
θ_k = transparency coefficient related to the k-th species

*PhD candidate, Department of Aerospace Engineering, Universidad Carlos III de Madrid, Leganés, Spain, sdallefa@ing.uc3m.es
†Assistant professor, Department of Aerospace Engineering, Universidad Carlos III de Madrid, Leganés, Spain, jiewei.zhou@uc3m.es
‡Postdoctoral researcher, Department of Aerospace Engineering, Universidad Carlos III de Madrid, Leganés, Spain, jperales@ing.uc3m.es
§Full professor, Department of Aerospace Engineering, Universidad Carlos III de Madrid, Leganés, Spain, eduardo.ahedo@uc3m.es
¶Senior scientist, Institute of Experimental Physics 1, Justus Liebig University Giessen, Heinrich-Buff-Ring 16, 35392 Giessen, Hesse, Germany, Kristof.Holste@physik.jlug.de

Copyright 2024 by the Electric Rocket Propulsion Society. All rights reserved.

I. Introduction

Among the electric propulsion systems, Ion Thrusters (ITs) and Hall Effect Thrusters (HETs) are two of the most mature technologies. The first, in particular, is characterized by a very high specific impulse I_{sp}, which leads to lower propellant consumption [1]. However, the typical design of an IT requires an internal thermionic hollow cathode to sustain the discharge [2]. This component is particularly complex and reduces the lifetime of the thruster, hence, alternatives have been investigated.

In the 1960s, Horst W. Loeb at Giessen University proposed a new design in which plasma is sustained by electromagnetic fields [3, 4]. The thruster, named Radio-frequency Ion Thruster (RIT), uses an inductive plasma generator constituted by a radio-frequency (RF) antenna that is wrapped around the discharge chamber. Although the design has been studied for 60 years, the influence of geometrical and operational parameters on performance is not fully understood. The complex dynamics of the plasma inside the thruster and in the plume require intensive experimental investigations. However, empirical approaches are very expensive, and the regions they can study are limited, such as the discharge chamber. Therefore, numerical simulations are essential for providing deep insights at a moderate cost. Moreover, simulations are highly effective for parametric analyses involving geometric parameters, where each variation represents a different thruster.

A scheme of the thruster is shown in Fig.1. The RF antenna usually takes an input frequency of a few MHz to heat the electrons via the interaction with electromagnetic waves. Neutral particles are injected with a gas inlet and are ionized through energetic electron bombardment inside an insulated chamber. A gridded extraction system accelerates then the produced ions in low-divergent beams with very high velocity, thus high I_{sp}. The design, although does not present an internal hollow cathode, still requires an external neutralizer to eject an electron current equal to the ion beam current I_{beam}. This component is essential to avoid charge imbalances. A RIT can be divided into 3 different regions [5]: the plasma generator, the

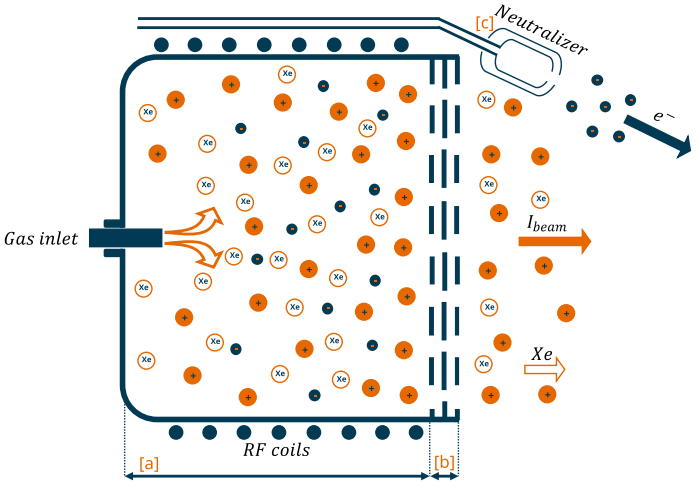

Figure 1: Scheme of a RIT

ion accelerator, and the electron neutralizer respectively indicated in the scheme with [a], [b] and [c]. Each region is affected by different parameters that can be related to the geometry of the structure or to operative conditions. Separating between different regions is essential because thruster behavior relies on the intricate interplay among them. The most appropriate method for modeling thrusters should involve a unique self-consistent simulation that includes key components such as the radio-frequency generator (RFG), discharge chamber, and extraction system. This approach has been used in some particular cases with a very small thruster [6], but for bigger domains, it can be very difficult and computationally heavy. Thus, the typical procedure is to separate the regions by modifying some inputs or boundary conditions to address the missing parts.

This paper aims to analyse the plasma inside the discharge chamber of a RIT by adapting an existing simulation tool. To provide preliminary data and demonstrate the effectiveness of the model, the RIT-4, developed at Giessen University [7, 8], has been selected for the study. The device is a μN-thruster with a diameter of $\sim$ 4 cm and xenon as propellant. The small size and the large amount of data available make

Copyright 2024 by the Electric Rocket Propulsion Society. All rights reserved.

this thruster a very good candidate for numerical modelling. Indeed, Dietz et al.[9] and Reeh et al.[10] have tested and studied the RIT-4 with both experiments and simulations. In particular, the numerical analysis published in both works has been obtained by employing a global model. This typology of codes allows for preliminary prediction of averaged plasma magnitudes with a relatively low computational cost. A brief summary of the main characteristics offered by the code is given later in this paper.

The study proposed in this work is performed by HYPHEN, an in-house code developed at Universidad Carlos III de Madrid for simulating 2D axisymmetric plasma discharges [11, 12], which has been extensively used to study HETs and electrodeless plasma thrusters with magnetic nozzles [13, 14, 15]. By using HYPHEN, it is possible to analyse the thruster without assuming averaged-uniform quantities, thereby increasing the fidelity of the simulations. This approach can enhance and deepen the understanding of the complex interactions within the discharge chamber.

The paper is structured as follows. Section II gives a brief discussion of experiments and modelling at Giessen University. Section III is dedicated to the introduction of HYPHEN, its main features and the setup used in this study. In section IV, the results obtained with HYPHEN are provided, highlighting the main magnitudes that characterize the plasma discharge. Finally, section V shows the comparison between the two numerical models for densities, power losses, and spatial profiles.

II. The RIT-4: thruster and simulation

A. Info about RIT-4 and test facility

The Giessen RIT-4 belongs to the class of gridded ion thrusters and generates its plasma by inductive heating of the plasma electrons. The coil wound around the plasma has six turns with a slope of 5 mm per turn. The discharge vessel has a diameter of 21.5 mm and a length of 41 mm. The extraction system consists of three grids with a total of 151 extraction channels in hexagonal arrangement. The thickness of the acceleration and deceleration grids is 1 mm, while that of the screen grid is 0.5 mm. The grid spacing is 0.75 mm. The diameters of the screen, acceleration, and deceleration grids are 1.9, 1.2, and 1.9 mm, respectively.

The experimental investigations of the RIT-4 were conducted in the BigMac test facility, situated at the Institute of Experimental Physics 1 of the Justus Liebig University Giessen. The test facility has a length of 3 m and a diameter of 1.6 m. The facility is equipped with two cryogenic pumps, which enable the generation of a pumping speed of approximately 34,000 l/s in relation to xenon. It is assumed that the gas backflow into the thruster due to the background gas is negligible, given the pumping speed and typical mass flows for a thruster of this small size. The RIT is located on an ISO-K-160 flange, which is mounted in the centre of the dished end of the test facility. The plume is thus orientated along the axis of symmetry of the cylindrical test facility. At the conclusion of its trajectory, the ion beam impinges upon a target comprising inclined graphite plates, thus reducing the backflow of sputter particles.

The screen and acceleration grids are supplied with high-voltage power supply units from Fug, while the RFG is supplied with a power supply unit from TDK-Lambda. The deceleration grid is grounded via the chamber wall of the test facility; a neutraliser was not employed. The propellant supply of the thruster was realised with the assistance of a Bronkhorst mass flow controller. A Pearson 2878 probe was employed to monitor the coil current. During the operation of the thruster, a beam current controller implemented using LabVIEW software was utilised to ensure a constant beam current. The corresponding programme employs the PID routines of LabVIEW and regulates the RFG power to maintain a constant beam current.

B. Info about global model

The Giessen global model is based on the work of Chabert [16] and was further developed by Dietz et al. and Reeh et al. Various model types are now available in Giessen, which differ in terms of their modelling assumptions. Pure 0D models make global volume-averaged assumptions about the underlying physical interactions. Although this approach ensures that the computer performance required to solve the relevant rate equation systems for mass conservation, charge conservation and power balance is kept to a minimum, certain geometric effects, such as the non-axiality of the magnetic field due to the gradient of the coil, cannot be modelled correctly. This can be better realised with 2D axisymmetric or 3D codes, for example. In the 3D code, the grid transparency for ions and neutral particles is calculated using an ion extraction model (either via IGUN or via software developed in-house) and direct simulation Monte Carlo Collision methods.

Copyright 2024 by the Electric Rocket Propulsion Society. All rights reserved.

The spatial distribution of the ion density is weighted with two factors:

$$h_L = \frac{0.86}{\sqrt{3 + \frac{L}{2\lambda_i}}} \tag{1}$$

for axial direction and

$$h_R = \frac{0.8}{\sqrt{4 + \frac{R}{\lambda_i}}}, \tag{2}$$

for radial direction introduced by Chabert [17] and Lieberman [18]. The requisite thruster parameters are computed using the corresponding calculation sequences, which are detailed for all model types in [9].

III. Methodology

The comparison and the analysis presented in this work are obtained with HYPHEN by introducing the modeling for the grid extraction system. HYPHEN is an axisymmetric hybrid code to simulate plasma discharges in different electric thrusters. The hybrid formulation consists of a model where heavy particles (ions and neutrals) are simulated with a particle-in-cell (PIC) approach while electrons are treated with a fluid approach. The structure of HYPHEN can be summarized into 3 different modules: the ion module implements the PIC model and computes the dynamics of heavy species by discretizing their distribution functions as macroparticles and using Monte Carlo Collision methods; the electron module implements the fluid model and solves drift-diffusive equations (for current, momentum and energy) while imposing quasi-neutrality; and a sheath module that accounts for the interaction between walls and quasi-neutral plasma. The outputs of the ion module are the density n_s and velocity $\boldsymbol{u}_s$ for a heavy species s; and those of the electron module are the electric potential ϕ, electron current density $\boldsymbol{j}_e$ and electron temperature T_e. The following description of HYPHEN underlines only the most relevant characteristics for this work. More detailed descriptions of the modules can be found in Refs. [13, 15, 19, 20].

The discharge chamber has been simulated independently by approximating the entire extraction system as a single semi-transparent surface. This exit section of the domain can function as a material boundary where ions are recombined and neutrals are reflected, or as an open boundary that allows heavy particles to exit the domain. The effect is governed by a set of transparency coefficients, θ_n for neutrals and θ_i for ions. If a macro-particle interacts with a semi-transparent cell, a random number is generated. If this number is lower than the transparency, then the boundary cell is considered as free-loss, otherwise as material surface. It is crucial to differentiate the transparency coefficients between ions and neutrals since the first species is mainly affected by the screen grid, while the second by the acceleration grid, which usually presents a different geometry. Considering a statistical approach, the semi-transparent surface is an efficient way to approximate the extraction system. Anyway, this boundary condition does not simulate the plasma sheath close to the screen grid's holes, which is responsible for the meniscus shape affecting the ion optics. For this reason, imposing an ion transparency coefficient means assuming the shape of the sheath. The simulations presented in this work are performed by using geometrical transparency for both screen and acceleration grids, thus the fraction corresponding to the open area of the grids. The assumption implies a planar sheath through the holes. Moreover, both θ_n and θ_i are assumed to be uniform over the entire exit section with respective values of 30 % and 5 %.

Fig. 2 shows a sketch of the simulation. The simulated domain is cylindrical with a radius of 21.5 mm and an axial length of 41.0 mm. The propellant for the operation is Xe, and two populations, neutrals and singly charged ions generated from ionization are simulated. At the back wall, an injection surface is placed with a radius of 4 mm; a mass flow rate of neutrals is injected with a mean velocity of 180 m/s and a temperature of 300 K. The back wall and the lateral wall are dielectric, while the right wall is semi-transparent and metallic. Neutrals reaching the walls are reflected, and ions are recombined and reflected; the angle after reflection is given by the Schamberg model, while the energy is assumed accommodated with a coefficient α_w of 85 % [21]. For the electrons, at the dielectric walls, the electron current normal to the wall j_{ne} is imposed equal to the opposite of that for ions $-j_{ni}$. At the right metallic wall, the electron current absorbed by the screen grid $I_{e,s} = \int_s j_{ne} dS$ is equal to:

$$I_{e,s} = -(I_{i,s} + I_{beam}) \tag{3}$$

Copyright 2024 by the Electric Rocket Propulsion Society. All rights reserved.

where $I_{i,s}$ is the ion current collected at the screen grid and I_{beam} is the ion current in the beam downstream. The potential of the grids ϕ_s is adjusted with respect to the plasma (the reference potential is imposed at $(z, r) = (0, 0)$cm) to fulfill such current balance. The sheath developed near these walls is solved with a model accounting for secondary electron emission and partial depletion of the tail of electron velocity distribution function [13, 20].

Fig.2 also presents the mesh used in this study, where cell size is around 1 mm. PIC codes typically present a very fine mesh, which highly affects the computational time. The requirement is imposed by the Debye length that can be in the order of $10^{-5} \sim 10^{-4}$ m for these thrusters. However, HYPHEN simulations are not impacted by this threshold since the fluid module assumes quasi-neutrality over the entire domain. Thus, the mesh needs only to satisfy the CFL condition [22] ensuring that macro-particles do not cross more than one cell per PIC time-step. The target number of macroparticles per cell is 100, which assures good statistics.

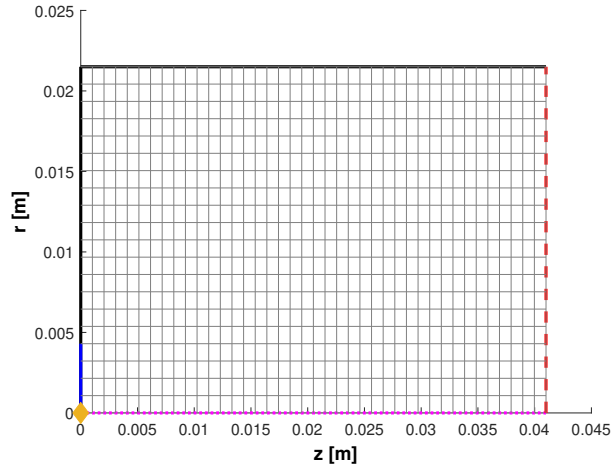

Figure 2: Domain representation with mesh and boundary conditions. The injection surface is highlighted in blue, contrasting with the dielectric walls depicted in black. A red dashed line delineates the semi-transparent surface, while the axial line is denoted in magenta. A yellow diamond indicates the node considered as reference potential

The considered power balance can be expressed by the following equation:

$$P_{rf} = P_{wall} + P_{inel} + P_{out} \tag{4}$$

where P_{wall} is the plasma energy flow lost at the walls; P_{inel} is the power loss due to inelastic collisions (ionization and excitation); and P_{rf} is the power deposited inside the discharge chamber. The RFG is not simulated, P_{rf} describes the power that is directly absorbed by the plasma and it is defined by an input power density map Q_a. The simulations presented in this work have been computed by assuming a uniformly distributed power deposition along the entire domain. Finally, P_{out} is the energy associated with the ions that are leaving the domain across the semi-transparent surface. This value does not represent the beam power P_{beam}, which can be expressed as:

$$P_{beam} = I_{beam} \cdot \phi_{\infty,s} \tag{5}$$

where $\phi_{\infty,s}$ is the potential drop between the screen grid and the region far away from the thruster. Indeed, with the depicted setup, the acceleration grid and the potential drop in the extraction system are missing. Thus, ions leaving the domain are not accelerated and P_{out} does not correspond to P_{beam}. Since the details of the grids are not simulated, the power balance has only to consider P_{out}.

IV. Results of HYPHEN's simulations

A. Analysis of the plasma discharge

In this section, the results of the HYPHEN simulation analysis are presented, conducted with two mass flow rates, 63 and 108 μg/s, and two power levels, 10 and 50 W. All values are at steady state and have been

Copyright 2024 by the Electric Rocket Propulsion Society. All rights reserved.

time-averaged to minimize the numerical noise typically encountered in PIC and hybrid codes.

Fig.3 illustrates the 2D contour maps of the most important plasma magnitudes. Specifically, (a) and (b) are related to ion density n_i at low and high power, while (c) and (d) depict the neutral density n_n inside the domain. As expected, at low power, the ionization level is poor, and the ions are concentrated in the center of the discharge chamber. The profiles are comparable and the electron temperatures at 63 and 108 μg/s are respectively of 3.5 and 3.0 eV. Both simulations present a similar neutral distribution, i.e. a peak value close to the injection and an almost uniform distribution all over the domain. However, by increasing the power, ion density significantly changes. Indeed, the maximum value moves from the center towards the injection surface, where n_n is higher. This effect is more pronounced in the low mass flow rate scenario, which exhibits a T_e of 7.7 eV, nearly double the 4.1 eV observed with a high $\dot{m}$. Neutral profiles, instead, are less influenced by input power and they preserve their uniform distribution. Little changes can be observed in the low mass flow rate case, where there is a low density region in the center of the chamber. In (e) and (f) the electric potential ϕ is displayed. Notice that the data presented do not represent values at the boundaries. Predictably, the potential map follows the ion's density profiles, moving towards the injection surface as the electron temperature increases.

Fig. 4 (a),(b),(c) and (d) show the ion and electron current density maps with associated streamlines. When comparing equal mass flow rates and powers, j_i and j_e profiles are very similar. Streamlines show that most of the current goes to the lateral boundaries, which suggests a high level of ion recombination and wall losses. Belong the current reaching the semi-transparent surface, only a fraction equal to the screen grid transparency composes the effective beam current.

Some further considerations can be made from Fig.5. The plots show power losses and ionic current composition with respect to the input power in two different mass flow rate scenarios. Indeed, the right figure shows the ion current loss at the walls I_{wall} and I_{beam}. The latter has been multiplied by a factor of 10 for clarity. It is evident that moving towards high P_{rf}, most of the ions and, thus, of the power, go to the walls. This suggests that the characterization of boundaries has a strong influence on the simulation results. Another important consideration regards the beam current. Analyzing the case with $\dot{m} = 63\mu$g/s, I_{beam} and I_{wall} increase with the input power until ~ 45 W. After this value, both currents are almost flat, which indicates a very high utilization efficiency and that only a very small fraction of the additional input power produces ions for thrust. At low power, instead, it is interesting to notice that different mass flow rates converge into a unique value due to the low ionization level. Studying the energy loss composition, the inelastic ones are prevalent at low P_{rf}, where temperatures are lower. By moving towards higher powers, P_{inel} reaches an almost constant value of 15 and 30 W respectively for 63 and 108 μg/s. In this regime, wall losses strongly rise, becoming the prevalent source of power dissipation.

To better understand the magnitudes at the boundaries, it can be useful to analyse wall values. For this analysis, a radial-axial variable ξ has been introduced. ξ is a coordinate that starts in the potential reference point and follows the material boundary of the domain, ending in the bottom right corner, where the semi-transparent surface crosses the central axis. Results are presented in Fig.6. In particular, the first row represents ion and electron current going towards the walls, i.e. j_{ni} and j_{ne}, while the last two plots indicate the wall energy fluxes. Data are presented for 63μg/s and two different input power: 10 and 50 W. For these two configurations, the obtained steady-state potentials at the grids are respectively -20 and -48 V. Values are constant since the surface is metallic. The difference reflects the electron temperature, which is significantly higher at 50 W.

j_{ne} is evaluated from the contribution of the flux of primary electrons going towards the wall and the ones emitted from the wall due to secondary electron emission (SEE). By looking at the currents, one observation is that j_{ni} and j_{ne} are exactly the opposite for the majority of the simulation domain. This comes from the dielectric boundaries, which assume an electron current density equal to the ion's one at each cell. The curves deviate on the semi-transparent metallic surface, enforcing a condition of zero net current. The graph shows that in this region, the electron current density remains uniform across the surface, a point that merits discussion. Inside the domain, the electron temperature is almost constant since the magnetic field is absent and the electron conductivity is very high. Therefore, the potential can be derived from the Boltzmann relation:

$$\phi = \phi_0 + \frac{T_e}{e} \ln\left(\frac{n_e}{n_{e,0}}\right) \tag{6}$$

where ϕ_0 and $n_{e,0}$ are respectively the electric potential and density at the reference point. e indicates the elementary charge and T_e the electron temperature in Joule. j_{ne}, instead, is evaluated using the collisionless

Copyright 2024 by the Electric Rocket Propulsion Society. All rights reserved.

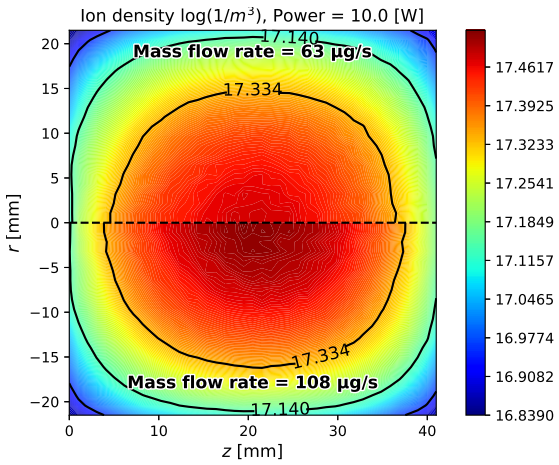

(a) n_i comparison with 10 W

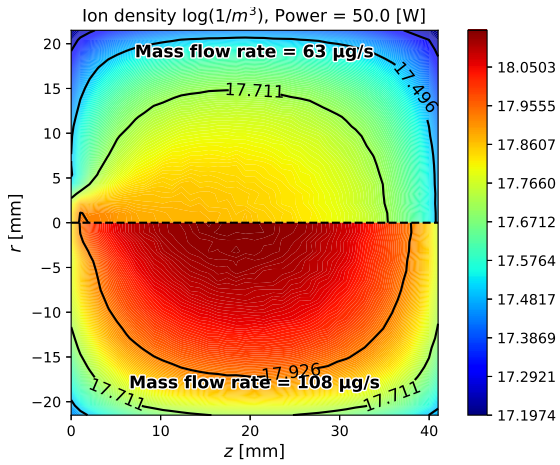

(b) n_i comparison with 50 W

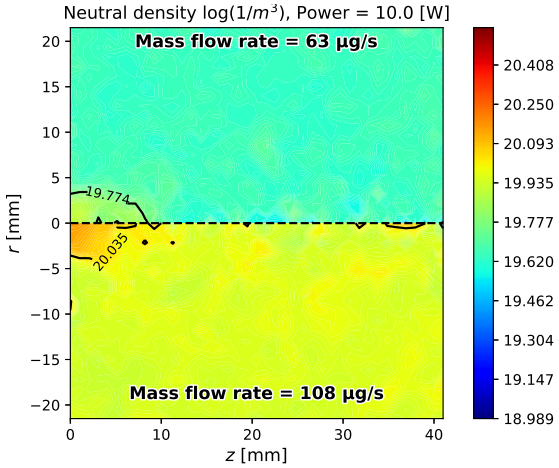

(c) n_n comparison with 10 W

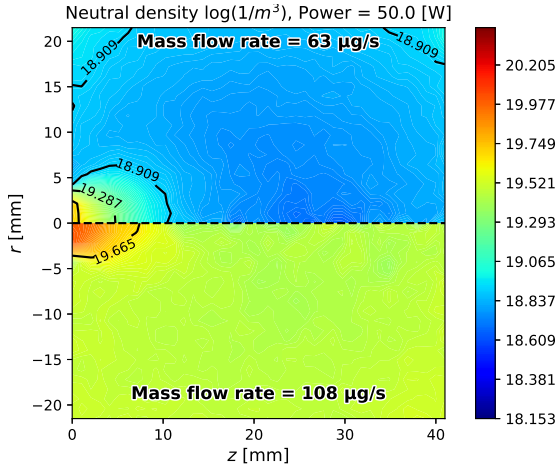

(d) n_n comparison with 50 W

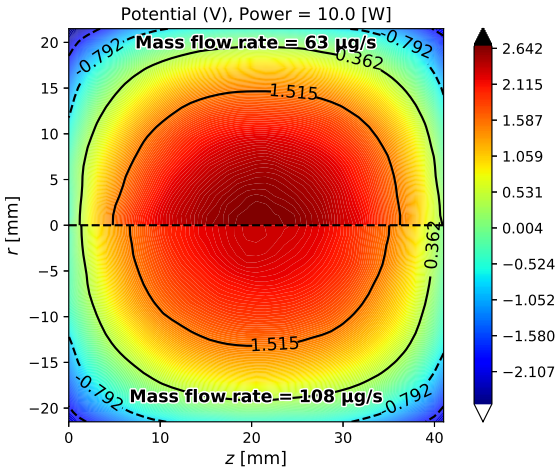

(e) ϕ comparison with 10 W

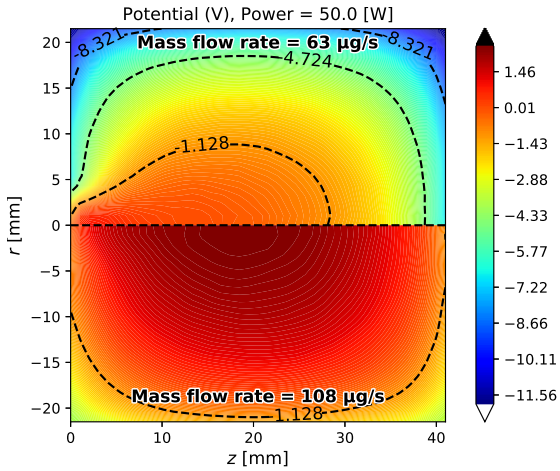

(f) ϕ comparison with 50 W

Figure 3: 2D maps of ion density, neutral density and electric potential inside the discharge chamber for different mass flow rates at 10 and 50 W

Copyright 2024 by the Electric Rocket Propulsion Society. All rights reserved.

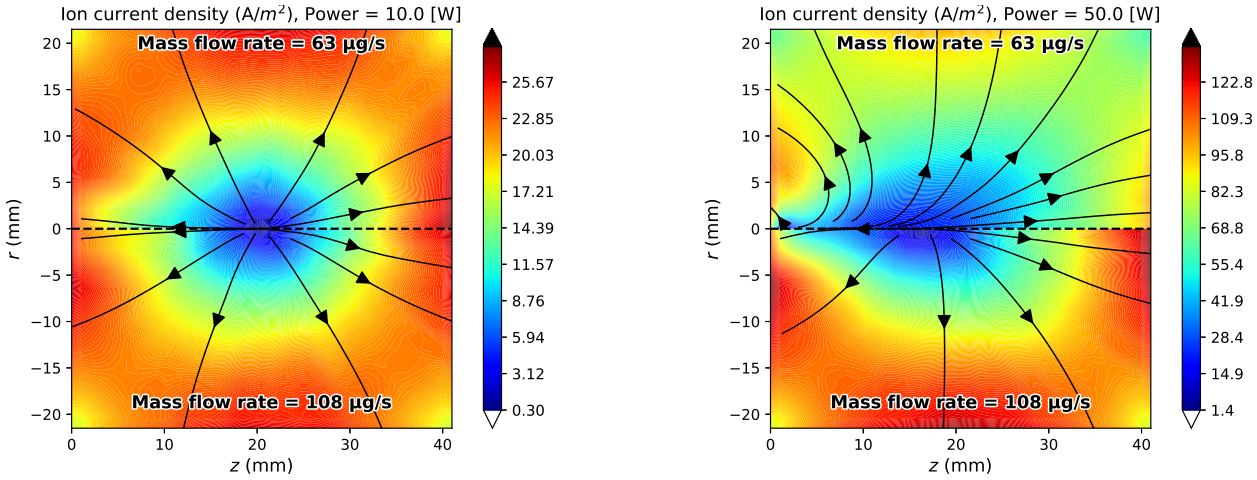

(a) j_i comparison with 10 W

(b) j_i comparison with 50 W

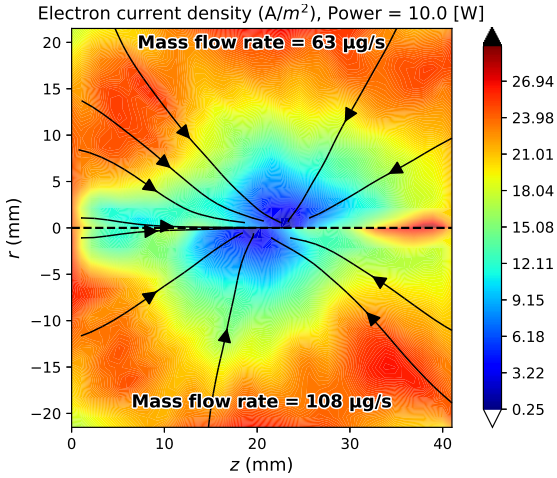

(c) j_e comparison with 10 W

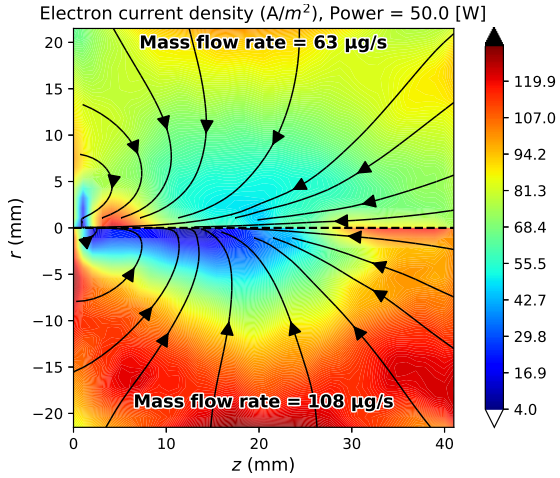

(d) j_e comparison with 50 W

Figure 4: 2D maps of ion current density and electron current density inside the discharge chamber for different mass flow rates at 10 and 50 W

sheath model with a Maxwellian distribution function, described as follows:

$$j_{ne} = en_{e,s}\exp\left(e\frac{\phi_s - \phi_{se}}{T_e}\right)\sqrt{\frac{T_e}{2\pi m_e}} \tag{7}$$

with m_e as the electron mass and ϕ_{se} as the potential at the sheath edge. Since the grid system is metallic, ϕ_s is constant, hence, substituting ϕ_{se} from equation 6 into 7 the electron density at the sheath edge $n_{e,s}$ cancels out, resulting in a constant current density profile. j_{ne} at the grids is then multiplied by $1-\theta_e$, where $\theta_e = \theta_i$ represents the electron transparency. This modification ensures that the code accurately reflects the influence of the open sections of the grids on the electron current density.

Considering the ion current density, j_{ni} is lower when close to the outer boundary and higher close to the central axis. The two regions seem to be unbalanced, with a prevalence of ionic current. However, it is important to highlight that the area is not linear with the x-axis. Indeed, moving from $\xi = 60$ to $\xi = 80$ mm, the plotted values are related to those regions that are closer to the central axis, hence with a lower area. Another important observation is that the shapes of the curves for currents are almost the same. Increasing the power doesn't seem to significantly change the profiles. The main difference is related to the region close

Copyright 2024 by the Electric Rocket Propulsion Society. All rights reserved.

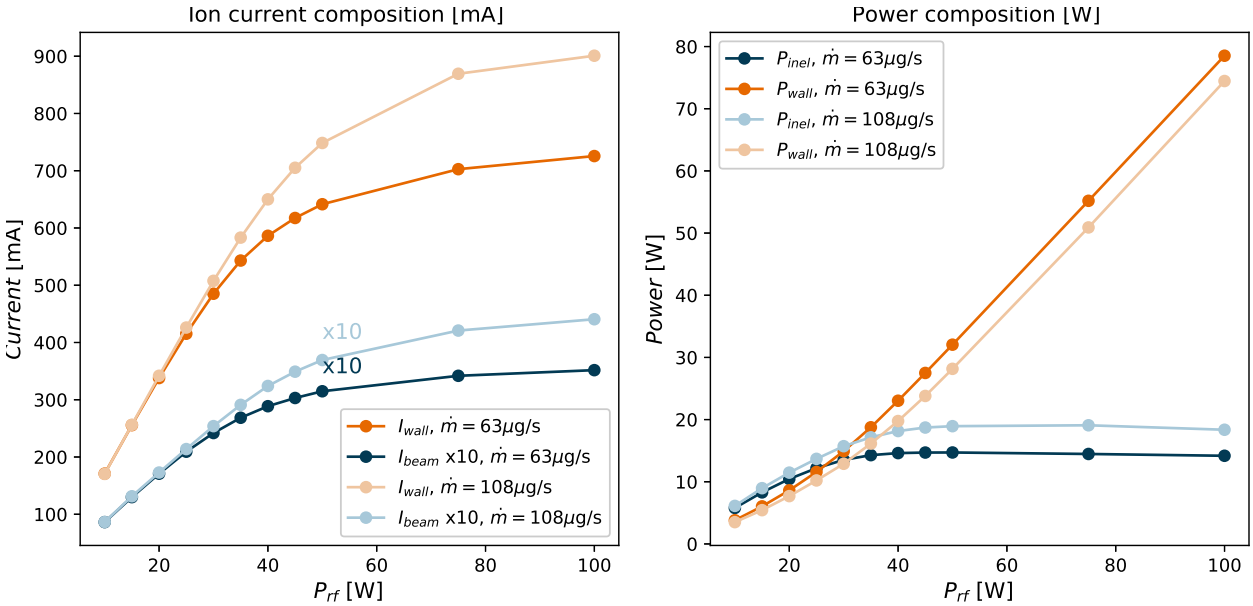

Figure 5: Ion current composition and power composition as functions of P_{rf} at mass flow rates of 63 and 108μg/s

to the injection surface. As shown in Fig.3 (b), higher levels of powers move the ion density peak towards the injection region. This explains the increased j_{ni} at 50 W and the presence of an additional maximum for $\xi \sim 9$ mm.

Plots in the second row show the energy fluxes to the walls. Figures indicate that most of the wall losses are related to ions. Indeed, ion energy P_i'' reaches even twice P_e'' value at low power and is more than the 75 % higher at 50 W. Even in this case, profiles do not change significantly by changing the power, but a little difference appears close to the injection surface due to the elevated ion and electron fluxes. Moreover, the grids manifest to be the region with superior losses. The plots also present the energy fluxes associated with neutral particles P_n''. Predictably, neutral kinetic energy is very low with respect to ion and electron contributions. At low power, P_n'' is negative for $\xi < 3$ mm, which indicates dominance of kinetic energy from the injected particles. Instead, when P_{rf} is 50 W, the fluxes are positive, pointing out a higher component coming from wall impacts.

B. Preliminary analysis of the effects of transparency on thruster efficiencies

The upcoming investigation aims to analyze the utilization efficiency η_u, the propulsive efficiency η_p and the thrust efficiency η_t for different transparency conditions. The three parameters are evaluated with the following equations:

$$\eta_u = \frac{\dot{m}_{i,\infty}}{\dot{m}} = \frac{I_{beam} \cdot m_{ion}}{\dot{m} \cdot e} \tag{8a}$$

$$\eta_p = \frac{P_{beam}}{P_{tot}} = \frac{I_{beam} \cdot \phi_{\infty,S}}{I_{beam} \cdot \phi_{\infty,S} + P_{rf}} \tag{8b}$$

$$\eta_t = \frac{F^2}{2P_{tot}\dot{m}} = \eta_u \cdot \eta_p \tag{8c}$$

In the equations, m_{ion} is the ion mass, here considered equal to xenon neutral mass. P_{tot} is the total input power, which considers both losses and power requested by the grid system to accelerate ions. It is important to underline that the input power parameter P_{rf} used in this work refers only to the losses inside the discharge chamber. $\phi_{\infty,S}$ has been obtained considering an artificial potential drop $\Delta V = -1350$ V. η_u represents the amount of injected propellant that is ionized and contributes to the beam current. Since doubly charged ions are not simulated in this work, $\dot{m}_{i,\infty} = I_{beam} \cdot m_{ion}/e$. The propulsive efficiency η_p, instead, indicates the percentage of total input power that is used for thrust, while η_t represents the global behavior

Copyright 2024 by the Electric Rocket Propulsion Society. All rights reserved.

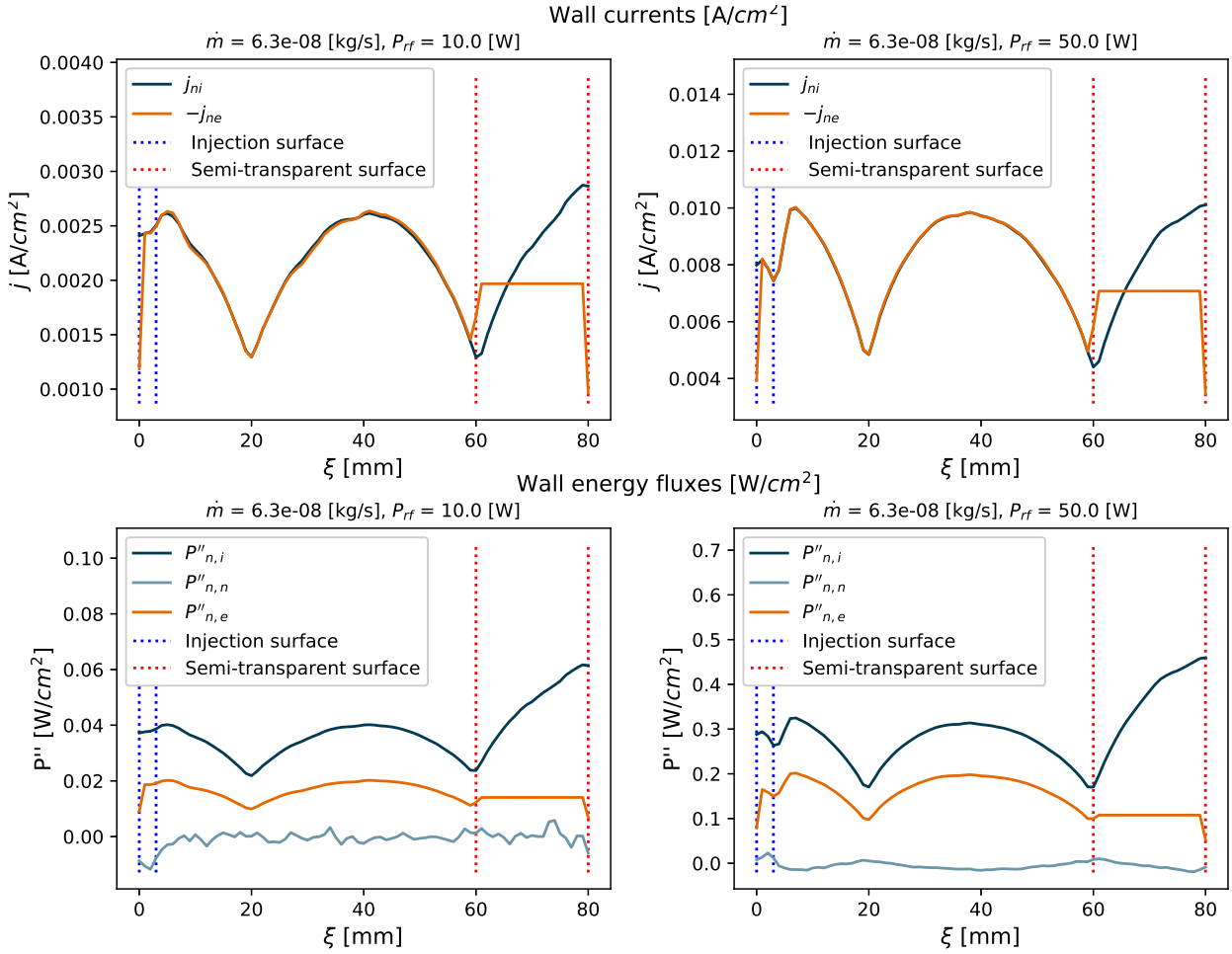

Figure 6: Current and energy flux at the wall for P_{rf} values of 10 and 50 W

of the thruster. Equation 8c assumes that η_t is affected only by utilization and propulsive efficiencies. In particular, the influences of other terms, such as the divergence efficiency, are neglected. In this work, ion optics effects are not considered and the focusing sheath is assumed to be planar. Consequently, ions are supposed to be exhausted with a purely axial velocity.

For this analysis, the transparency coefficients have been changed from the one given in III. The coefficients are named as $[\theta_i, \theta_n]$, respectively related to ions and neutrals in percentage. The study refers to a constant mass flow rate, equal to 78μg/s, and 3 different transparency setups: $[30, 5]$, $[40, 5]$ and $[30, 10]$. Fig.7 presents the three efficiencies and T_e as a function of the input power P_{rf}. The electron temperature is shown in the upper left figure. As expected, higher power results in an elevated T_e. From a transparency perspective, the highest temperatures are reached for bigger θs. However, the mechanisms that produce this effect are different. In case $[30, 10]$ a bigger amount of neutrals can leave the discharge chamber. As a consequence, the neutral density is lower, which implies lower inelastic losses. Since the deposited power is fixed, the electron temperature and wall losses have to increase according to equation 4. On the other hand, elevated values of θ_i lead to a lower level of wall recombination at the grids. This further reduces the neutral density, resulting in a higher T_e. The utilization efficiency, presented in the top right plot, shows a straightforward trend. As the input power increases, the ionization rate rises, resulting in a greater number of neutrals being ionized. Moreover, the cases with higher ion transparencies and lower θ_n present better values, as predicted by the theory [5]. Additional considerations can be made by analysing the propulsive efficiency η_p shown in the bottom left figure. At reduced power, the ionization level is very low for all tested cases, thus there are very few losses and P_{rf} is limited. However, when the electron temperature and the ionization level increase, the propulsive efficiency drops, which implies that losses, and in particular wall

Copyright 2024 by the Electric Rocket Propulsion Society. All rights reserved.

recombination, assume a prevalent role. Lower values of η_p are related to little ion transparencies and small θ_n. Indeed, since η_u is reduced, the setups are related to lower beam current. Thus, for the same input power, the best propulsive efficiency is associated with the transparency conditions that allow maximum utilization efficiency. Lastly, thrust efficiency is presented in the bottom right corner. The plot exhibits a curved behavior with a peak value. Trivially, since η_t depends on utilization and propulsive efficiency as expressed by 8c, better values are achieved for high ion and low neutral transparencies. In particular, θ_n demonstrates to have a very impacting effect on thruster performances, decreasing η_t up to $\sim 25\%$.

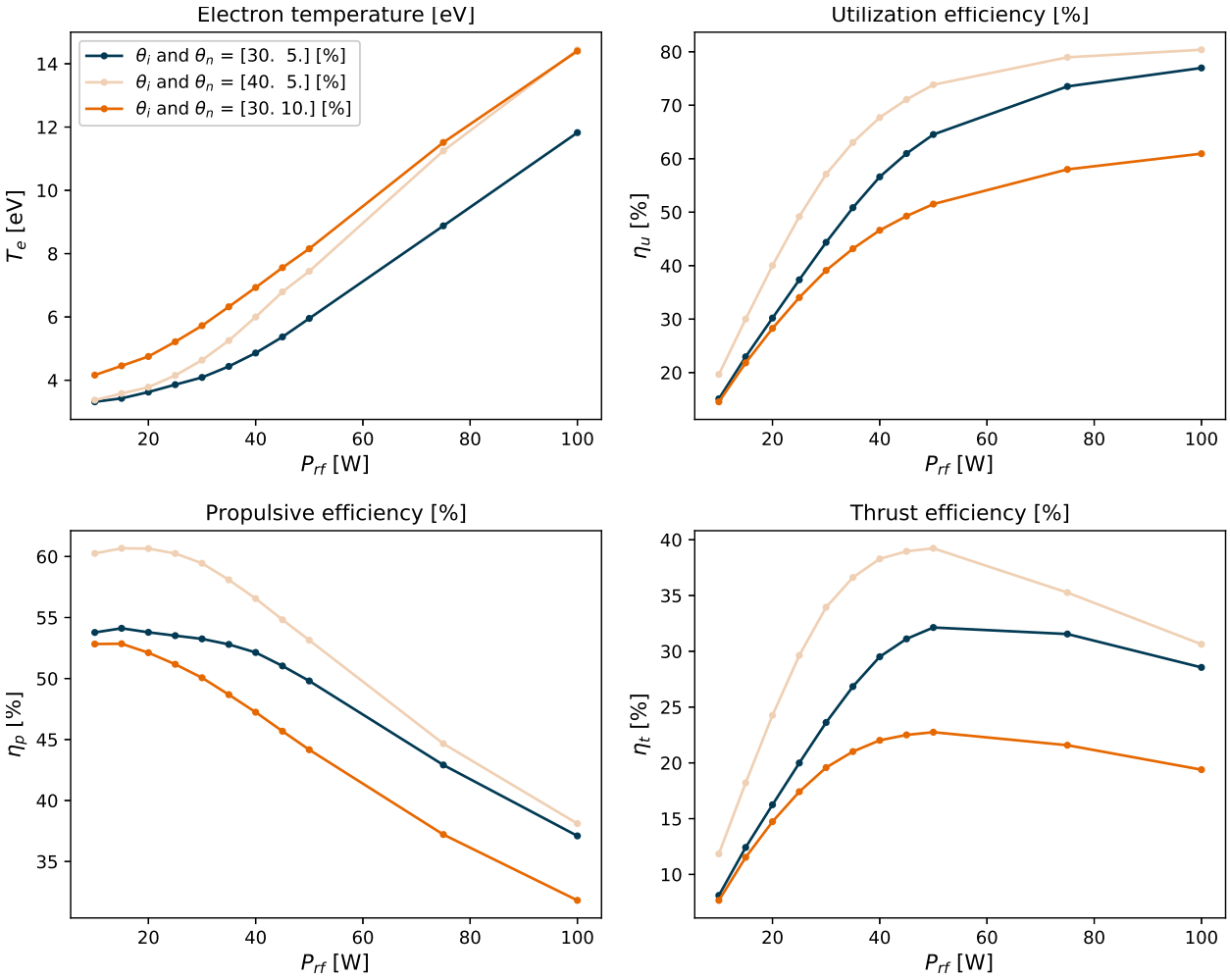

Figure 7: Utilization, propulsive, thrust efficiencies and electron temperature in relation to power and transparency

V. Comparison against densities, electron temperature and power losses at constant beam current

In this section, the simulations obtained with HYPHEN are compared against the results from Giessen. It is important to underline that the following comparison involves two numerical models, one of which has been validated.

Indeed, the published experimental data concern to measurements of the input power to the radio-frequency generator and the current in the coil. Since the hybrid model does not simulate the RFG, this section focuses on the numerical results obtained with the 3D global model. Finally, the density profiles computed by HYPHEN inside the chamber will be briefly discussed.

The global model can provide values by imposing the beam current as a set point. In HYPHEN, instead,

Copyright 2024 by the Electric Rocket Propulsion Society. All rights reserved.

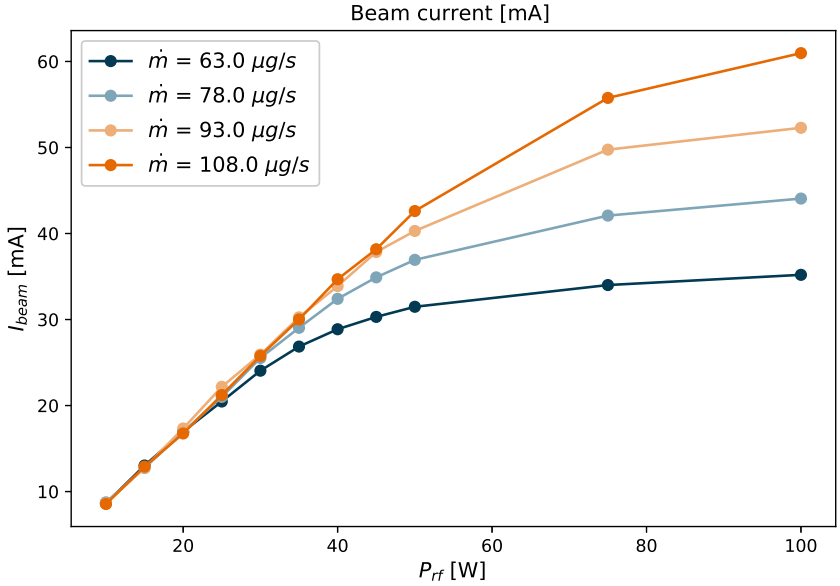

Figure 8: Beam current obtained at different input power and mass flow rate

I_{beam} is the output of the simulation. Hence, the following results have been obtained by interpolating simulations with different power and mass flow rates. In particular, the model comparison has been conducted by simulating 4 different mass flow rates with 11 different input powers. Fig.8 shows the obtained beam current for each combination. The interpolation provides a function of the beam current which is then computed at 10 mA and 30 mA, which are the conditions tested in the cited reference works.

The density comparison between the two models is presented in Fig.9. Global model data are indicated with "GM" and provide steady-state magnitudes of ion and neutral densities. However, while the latter is considered uniform, ion density is assumed with axial and radial profiles. This implies that the result provided in the plot represents the plasma bulk density $n_{i,0}$, which, as hypothesized by the profiles, reaches its maximum value at the center of the discharge chamber. In contrast, with HYPHEN, the bulk position is not constrained to the axial and radial center of the chamber. The maximum location has already been discussed in section IV. Therefore, the ion density reported is based on the peak density observed across the entire 2D domain. Neutral density, instead, is averaged over the entire volume.

Given these considerations, the comparison is highly favorable, and the two models are well-aligned in both scenarios. In particular, at 10 mA the steady state neutral density matches almost exactly the reference one. A bit worse is the neutral densities at higher beam currents, where values are underestimated. Regarding ion density, the references provide only data at 30 mA. In this case, the results given by HYPHEN estimate higher values, indicating that the peak value is more significant for the hybrid code. Data at 10 mA are shown for completeness. Anyway, since the neutral density matches very well the data, it is reasonable to think that values obtained from HYPHEN are not far from the reference.

Another comparison is the resulting electron temperature for different injected mass flow rates, as shown in the bottom left figure. In this case, both models display uniform values across the entire domain. The global model assumes this uniformity intrinsically, while in the HYPHEN model, the temperature is computed self-consistently but remains constant due to the high electron conductivity. Thus, spatial considerations are not needed in this analysis.

Upon examining the results, the condition that shows a very good agreement with the global model is the case with 10 mA of beam current. Instead, the comparison is less favorable at 30 mA. With this condition on I_{beam}, at low mass flow rates, the electron temperature is almost 1.5 eV higher, with a difference up to 30%.

The significant discrepancy at low $\dot{m}$ can be explained by looking at the ion density computed on the exit surface. The bottom right plot shows the average ion density in the cells next to the grid's section for different mass flow rates. Global model's data have been obtained by multiplying the bulk density by the

Copyright 2024 by the Electric Rocket Propulsion Society. All rights reserved.

two coefficients h_L and h_R described by equations 1 and 2. The plot indicates that the average ion density at the grid surface is lower for HYPHEN's simulations. However, I_{beam} is proportional to the incoming ion flux, thus to n_i and the ion velocity v_i. Since the comparison has been obtained by a fixed beam current, the hybrid code must compensate for the lower density with a higher velocity in order to keep constant the ion flux. Given that velocity is strongly dependent on electron temperature, as it is related to the plasma sheath at the wall and specifically to the Bohm velocity, an increased temperature is needed. This elevated temperature is essential to meet the beam current requirement. The figure also shows that by increasing the mass flow rate, the ion density at the grids becomes closer to the one predicted by the global model, which justifies the better agreement of the electron temperature.

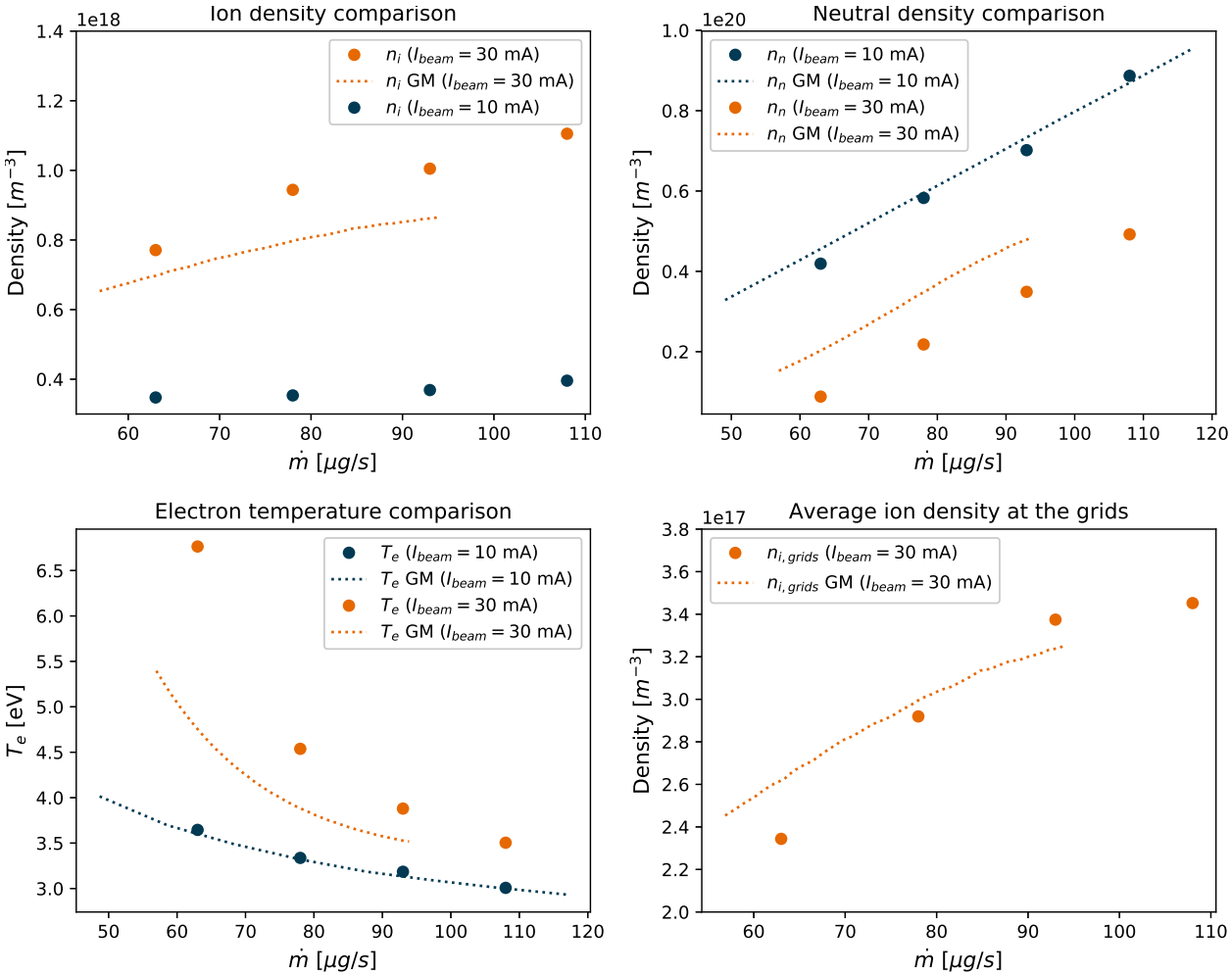

Figure 9: Model comparison at 10 mA and 30 mA for different input mass flow rates

The reference works present the power loss composition dividing between losses at the walls and by neutral exciting or ionizing collisions. The comparison is presented in Fig.10. Overall, the agreement is quite good, even if there are some differences in particular cases. Considering the values obtained for $I_{beam} = 10$ mA, wall losses are very close to the global model's one, which can be related to the well-alignment between the electron temperature in this case. Ionization and excitation losses are, instead, overestimated. The second, in particular, is estimated to be even 50% higher than the model. Since the collisional cross sections have been obtained from the same database and the electron temperature is very close, the difference is probably related to greater values of plasma densities.

Trends are generally compatible also with 30 mA of beam current. Even in this case, power losses due to ionization are almost independent of the neutral mass flow rate, while excitation losses increase. Comparing the power dissipated at the walls, the two trends are similar, but differences are in the order of 10%. Both plots present wall losses that decrease with $\dot{m}$. The explanation relies on T_e. As neutral density rises, the

Copyright 2024 by the Electric Rocket Propulsion Society. All rights reserved.

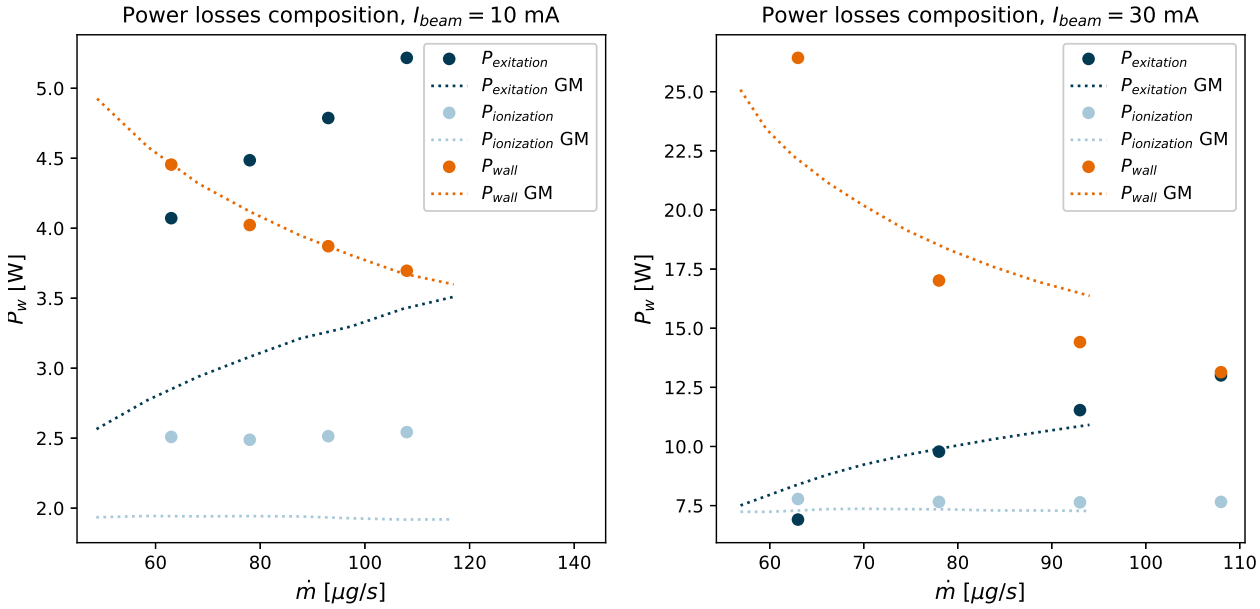

Figure 10: Comparison against reference power losses for different $\dot{m}$ and I_{beam} set at 10 mA and 30 mA

same ion flux at the grids, and thus the same beam current, can be obtained at a lower temperature. This reduction in temperature subsequently decreases wall losses.

A. Comparison against ion density at the wall

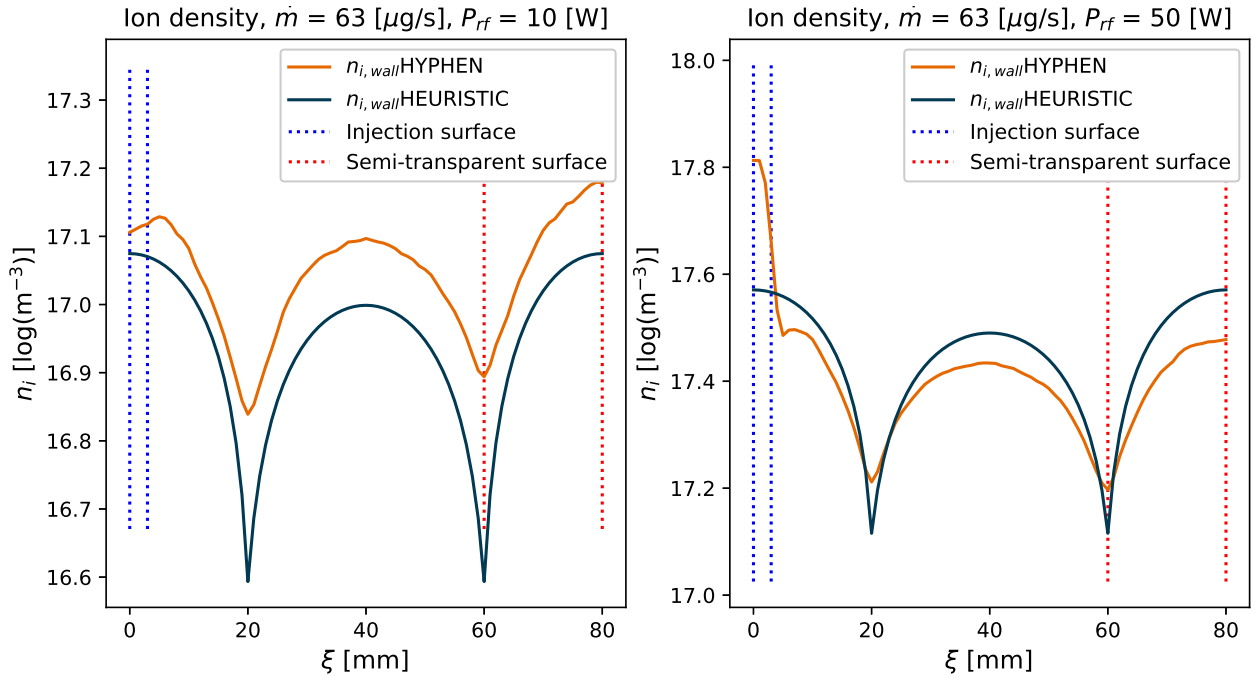

Figure 11: Comparison against ion density profile at the wall

This paragraph aims to briefly discuss the assumptions related to the radial and axial profiles assumed in the global model. The already mentioned sheath-to-bulk ratios h_L and h_R, formulated by Godyak are semi-empirical coefficients that can approximate the plasma density profile at low pressures [18]. HYPHEN, instead, does not assume a profile, thus it can be interesting to see under which conditions the heuristic

Copyright 2024 by the Electric Rocket Propulsion Society. All rights reserved.

formulations hold and when the difference becomes not negligible anymore. The comparison can also be interesting to define a possible explanation of the differences in terms of wall losses and electron temperature discussed before.

To analyse this hypothesis, a comparison of the density profiles is presented in Fig.11. Since those data are used only to compute magnitudes and losses at the wall, the comparison will be focused on n_i evaluated at the boundaries. As in the previous section, a radial-axial coordinate ξ has been introduced. The plots show the ion density distributions obtained at the wall with the two models at constant mass flow rates and 2 different input powers. Heuristic values have been computed by multiplying HYPHEN's peak density with the H-function described in [9] i.e.

$$h = \sqrt{1 - \left(\sqrt{1 - h_R}\frac{r}{R}\right)^2} \cdot \sqrt{1 - \left(\sqrt{1 - h_L}\frac{l}{L}\right)^2} \tag{9}$$

Considering the case where P_{rf} is 10 W, it is possible to see that the plot between HYPHEN and Godyak's profiles is in a good match. The main differences are located at the corners, where the hybrid code estimates higher values, while errors are contained below 25% on lateral sides. Discrepancies become noticeable at high power as presented in the right plot. Indeed, the ion profile starts to deviate significantly from the heuristic formulation near the injection surface. Specifically, as detailed in IV, the ion density peak shifts towards the injection point according to the hybrid model simulation, indicating elevated density in that region. For the remainder of the domain, differences are relatively limited.

VI. Conclusions

With this work, the first simulations of the discharge chamber of a RIT with HYPHEN have been presented. The hybrid code with the newly implemented semi-transparent surface allowed us to have a more detailed overview of what happens inside the chamber of the RIT-4, to better understand which are the key parameters for optimal performances. The setup has been tested for different injected mass flow rates and input power, showing the influence of those parameters on plasma magnitudes. The analysis also demonstrates the strong effects of wall losses, especially at high power, providing an indicative order of magnitude of those values. In particular, it has been proved that the wall energy flux is mainly affected by ion contribution. A preliminary analysis of the influence of transparencies provided performance in agreement with the theory, i.e. optimal conditions for lowest neutral and highest ion transparencies.

The comparison against Giessen's global model showed a very good agreement of HYPHEN for densities, electron temperature and power loss composition. The main differences have been qualitatively discussed and analysed. Moreover, the global model assumption of axial and radial profiles for the ion density has been studied and compared against the results of HYPHEN computed at the walls. The comparison demonstrated that the profiles represent a good hypothesis at low power, while are less effective at 50 W close to the injection surface.

Future analysis will play with geometry and operative conditions to provide useful insight for building more efficient RITs. The accuracy of the simulations will be improved by releasing the hypotheses of uniform power distribution and constant transparency coefficients. This will be done by coupling with external codes to simulate the radio-frequency waves plasma interactions and ion optics. Moreover, since many parameters have been demonstrated to affect the thruster's behaviour, sensibility analysis for variables such as the neutral injection temperature or the wall accommodation coefficient is needed.

Acknowledgments

This work has been supported by the R&D project PID2022-140035OB-I00 (HEEP) funded by MCIN/ AEI/10.13039/501100011033 and by "ERDF A way of making Europe"

References

[1] G.P. Sutton and O. Biblarz. *Rocket propulsion elements*. John Wiley & Sons, 2010.

[2] J. Sovey et al. "Development of an Ion Thruster and Power Processor for New Millennium's Deep Space 1 Mission". In: (Jan. 1998). DOI: 10.2514/6.1997-2778.

Copyright 2024 by the Electric Rocket Propulsion Society. All rights reserved.

[3] H.W. Loeb. "State of the art and recent developments of the radio frequency ion motors". In: *7th Electric Propulsion Conference, Williamsburg, Virginia, USA*. 1969. DOI: 10.2514/6.1969-285.

[4] H.J. Leiter et al. "Evaluation of the performance of the advanced 200 mN Radio Frequency Ion Thruster RIT-XT". In: *38 th AIAA/ASME/SAE/ASEE Joint Propulsion Conference and Exhibit, Indianapolis, IN*. 2002.

[5] D.M. Goebel, I. Katz, and I.G. Mikellides. *Fundamentals of electric propulsion*. John Wiley & Sons, 2023.

[6] N. Joshi and C. Heiliger. "Particle-in-Cell simulation of radio-frequency ion thruster RIT-1.0". In: *Journal of Electric Propulsion* 3.1, 5 (Feb. 2024), p. 5. DOI: 10.1007/s44205-024-00067-0.

[7] D. Feili et al. "The µNRIT-4 Ion Engine: a first step towards a European mini-Ion Engine System development". In: *30th International Electric Propulsion Conference, Florence, Italy*. IEPC-2007-218. 2007.

[8] H.W. Loeb et al. "Development Of RIT-Microtrhusters". In: *55 th International Astronautical Congress; Vancouver; Canada*. 2004.

[9] P. Dietz et al. "Global models for radio-frequency ion thrusters". In: *EPJ Techniques and Instrumentation* 8.10 (2021). DOI: 10.1140/epjti/s40485-021-00068-5.

[10] A. Reeh, U. Probst, and P.J. Klar. "Global model of a radio-frequency ion thruster based on a holistic treatment of electron and ion density profiles". In: *The European Physical Journal D* 73.232 (2019). DOI: 10.1140/epjd/e2019-100002-3.

[11] A. Domínguez-Vázquez. "Axisymmetric simulation codes for Hall effect thrusters and plasma plumes". PhD thesis. Universidad Carlos III de Madrid, Leganés, Spain, 2019.

[12] Jiewei Zhou. "Modeling and simulation of the plasma discharge in a radiofrequency thruster". PhD thesis. Universidad Carlos III de Madrid, Leganés, Spain, 2021.

[13] Jesús Perales-Díaz et al. "Hybrid plasma simulations of a magnetically shielded Hall thruster". In: *Journal of Applied Physics* 131.10 (2022), p. 103302. DOI: 10.1063/5.0065220.

[14] A. Sánchez-Villar et al. "Coupled plasma transport and electromagnetic wave simulation of an ECR thruster". In: *Plasma Sources Science and Technology* 30.4 (2021), p. 045005. ISSN: 1089-7674. DOI: 10.1088/1361-6595/abde20.

[15] Pedro Jiménez et al. "Analysis of a cusped helicon plasma thruster discharge". In: *Plasma Sources Science and Technology* 32.10 (2023), p. 105013. DOI: 10.1088/1361-6595/ad01da.

[16] P. Chabert et al. "Global model of a gridded-ion thruster powered by a radiofrequency inductive coil". In: *Physics of Plasmas* 19 (July 2012). DOI: 10.1063/1.4737114.

[17] P. Chabert and N. Braithwaite. *Physics of radio-frequency plasmas*. Cambridge University Press, 2011.

[18] M.A. Lieberman and A.J. Lichtenberg. *Principles of plasma discharges and materials processing*. John Wiley and Sons, Hoboken, NJ, 2005.

[19] A. Domínguez-Vázquez et al. "Axisymmetric plasma plume characterization with 2D and 3D particle codes". In: *Plasma Sources Science and Technology* 27.10 (2018), p. 104009. ISSN: 0963-0252. DOI: 10.1088/1361-6595/aae702.

[20] J. Zhou et al. "Magnetized fluid electron model within a two-dimensional hybrid simulation code for electrodeless plasma thrusters". In: *Plasma Sources Science and Technology* 31.4 (2022), p. 045021. ISSN: 0963-0252.

[21] A. Domínguez-Vázquez et al. "On heavy particle-wall interaction in axisymmetric plasma discharges". In: *Plasma Sources Science and Technology* 30.8 (Aug. 2021), p. 085004. ISSN: 1089-7674. DOI: 10.1088/1361-6595/ac1715.

[22] C.K. Birdsall and A.B. Langdon. *Plasma Physics via Computer Simulation*. Bristol: Institute of Physics Publishing, 1991.

Copyright 2024 by the Electric Rocket Propulsion Society. All rights reserved.